atmosphere

Article

Optical and Physical Characteristics of the Lowest Aerosol Layers over the Yellow River Basin

Miao Zhang [1,*], Jing Liu [2], Muhammad Bilal [3,*], Chun Zhang [1], Feifei Zhao [1], Xiaoyan Xie [4,5] and Khaled Mohamed Khedher [6,7]

1 School of Environmental Science and Tourism, Nanyang Normal University, Wolong Road No.1638, Nan Yang 473061, China; zchun0192@nynu.edu.cn (C.Z.); zff@nynu.edu.cn (F.Z.)
2 Lingnan College, Sun Yat-sen University, Guangzhou 510275, China; liuj243@mail2.sysu.edu.cn
3 School of Marine Sciences, Nanjing University of Information Science & Technology, Nanjing 2100444, China
4 South China Sea Fisheries Research Institute, Chinese Academy of Fishery Sciences, Guangzhou 510300, China; m180200554@st.shou.edu.cn
5 College of Marine Science, Shanghai Ocean University, Shanghai 201306, China
6 Department of Civil Engineering, College of Engineering, King Khalid University, Abha 61421, Saudi Arabia; kkhedher@kku.edu.sa
7 Department of Civil Engineering, Institut Superieur des Etudes Technologiques, Campus Universitaire Mrezgua, Nabeul 8000, Tunisia
* Correspondence: zm_liesmars@whu.edu.cn (M.Z.); muhammad.bilal@connect.polyu.hk (M.B.)

Received: 17 September 2019; Accepted: 19 October 2019; Published: 22 October 2019

Abstract: Studying the presence of aerosols in different atmospheric layers helps researchers understand their impacts on climate change, air quality, and human health. Therefore, in the present study, the optical and physical properties of aerosol layers over the Yellow River Basin (YERB) were investigated using the CALIPSO Level 2 aerosol layer products from January 2007 to December 2014. The Yellow River Basin was divided into three sub-regions i.e., $YERB_1$ (the plain region downstream of the YERB), $YERB_2$ (the Loess Plateau region in the middle reaches of the YERB), and $YERB_3$ (the mountainous terrain in the upper reaches of the YERB). The results showed that the amount (number) of aerosol layers (N) was relatively large (>2 layers) in the lower part of the YERB ($YERB_1$), which was mainly caused by atmospheric convection. The height of the highest aerosol layer top (HT_H) and the height of the lowest aerosol layers base (HB_1) varied significantly with respect to the topography of the YERB. High and low values of aerosol optical depth (AOD) were observed over the $YERB_1$ (plain area) and $YERB_3$ (elevated area) regions, respectively. Population, economy, and agricultural activities might be the possible reasons for spatial variations in AOD. AOD values for the lowest aerosol layer were high—between 0.7 and 1.0 throughout the year—indicating that aerosols were mainly concentrated at the bottom layer of the atmosphere. In addition, the integrated volume depolarization ratio (0.15–0.2) and the integrated attenuated total color ratio (~0.1) were large during spring for the lowest aerosol layer due to the presence of dust aerosols. The thicknesses of the lowest aerosol layers (TL_1) did not vary with respect to the topographic features of the YERB. Over the sub-regions of the YERB, a significant positive correlation between the AOD of the lowest aerosol layer (AOD_1) and the thickness of the lowest aerosol layer (TL_1) was found, which indicates that TL_1 increases with the increase of AOD_1. In the whole YERB, a positive linear correlation between the N and HT_H was observed, whereas a negative correlation between N and the portion of AOD for the lowest aerosol layer ($PAOD_1$) was found, which revealed that the large value of N leads to the small value of $PAOD_1$. The results from the present study will be helpful to further investigate the aerosol behavior and their impacts on climate change, air quality, and human health over the YERB.

Keywords: aerosol layers; AOD; CALIPSO; Yellow River Basin

1. Introduction

Aerosols are colloids of fine solid particles or droplets in the air [1–3] and can come from natural sources, such as fog, dust, and sea salt, or anthropogenic sources, such as haze, black carbon, and smoke [4–10]. The aerodynamic diameters of these solid or liquid particles mostly range between 0.001 and 100 μm, while larger particles can precipitate, resulting in suspension, and mixing in the atmosphere [11]. The World Health Organization pointed out that particulate matters with aerodynamic diameters less than 10 μm (PM_{10}) can penetrate into the lungs to the deepest part of the bronchus (such as the bronchioles and alveoli), causing disease [12]. The previous study has pointed out a certain relationship between the aerosol extinction coefficient and lung cancer mortality [13]. Within the field of environmental science, the Intergovernmental Panel on Climate Change reported that atmospheric aerosols are responsible for one of the largest uncertainties in the estimation of climate forcing, and they can scatter and absorb solar shortwave and longwave radiation, directly affecting the Earth's radiation balance [14]. They can also act as cloud condensation nuclei, changing the cloud's physical characteristics, life cycle, and indirectly affecting the Earth's climate system [15–17]. Therefore, the long-term, accurate, and regular monitoring of aerosol optical properties must be carried out continuously. In China, an increase in industrial activities and urbanizations was observed in recent years with the rapid economic development. Increasing numbers of aerosol particulates have been discharged into the atmosphere, leading to frequent air pollution incidents [18]. In recent years, severe regional haze pollution events have occurred in China's Pearl River Delta, the Yangtze River Delta, the Beijing–Tianjin–Hebei city cluster (BTH), and the northwest region of China, and corresponding aerosol observations have been conducted [19–24]. Recently, China has experienced many severe air pollution events [9]; for example, the Yellow River Basin (YERB) has experienced serious local pollution emissions due to coal mining, urbanization, excessive coal consumption, and the development of heavy industry (such as iron, steel, and cement). However, scientific studies related to these events over the YERB are limited.

Ground-based sun photometers such as the Aerosol Robotic Network (AERONET) and Chinese Aerosol Remote Sensing Network (CARSNET) provide continuous observation of the physical and optical properties of aerosols for a long period [25–28]. However, the vertical distribution of aerosols cannot be obtained using site measurements (sunphotometer, nephelometer, aethalometer, and aerosol spectrometer, etc.). These instruments provide point-based aerosol information; however, information about aerosol vertical distribution is very important for understanding the quantitative characteristics of aerosols. In contrast, aerosol characteristics cannot be obtained at a large scale using in situ measurements, as these measurements are limited to the point locations. For these reasons, Light Detection and Ranging (LiDAR) has gradually become the preferred remote sensing technology for atmospheric aerosol observations [29,30]. LiDAR is an active remote sensing detector, which emits laser beams and uses the echo signal by the scattering effect between the laser beam and atmospheric aerosol particles to perform quantitative retrieval [31–33]. Therefore, LiDAR operates continuously during the night and day and provides the vertical distributions of aerosol particles. In addition, LiDAR has a high spatial resolution (covering the range from the Earth's surface to the stratosphere with meter resolution) and temporal resolution (repeating frequency can reach up to kilohertz). In addition, it has a high detection sensitivity, and the signal received range can reach more than 10 orders of magnitude [34,35]. NASA launched the Cloud-Aerosol LiDAR and Infrared Pathfinder Satellite Observation (CALIPSO), the first active remote sensing sensor in 2006. It acquires not only aerosol information over a large regional scale but also the vertical distribution of different layers of atmospheric aerosols, which provide a new outlook on aerosol observations [36,37]. Therefore, this study intends to use the CALIPSO satellite to investigate the optical and physical characteristics of the lowest aerosol layers over the YERB. As the lowest aerosol layers are close to the ground surface and strongly related to human activities, it is, therefore, necessary to understand the physical and optical characteristics of the lowest layers of aerosols. However, only a few studies have been conducted over the region using optical remote sensing data [38,39], and no one has focused on the vertical distributions of the physical and optical properties of aerosol layers over the YERB. In addition, these have not characterized aerosols into different layers. To the best of our knowledge, this is the first study that has investigated different aerosol optical properties and their vertical distributions. Therefore, the objective of this study is to provide an understanding of the characteristics of the lowest aerosol layers over the YERB using the CALIPSO level 2 aerosol layer product from 2007 to 2014. The paper is organized as: the study area is discussed in Section 2, the materials and methods are described in Section 3, the results are discussed in Section 4, and the conclusions are provided in Section 5.

2. Study Area

Figure 1 shows a topographic map of the YERB region, which is located at 30° N–45° N, 95° E–120° E, including the plains in the downstream reaches of the YERB ($YERB_1$: 31° N–42° N, 112° E–119° E), the Loess plateau region in the middle reaches of the YERB ($YERB_2$: 32° N–43° N, 105° E–112° E), and the mountainous terrain in the upstream reaches of the YERB ($YERB_3$: 30° N–39° N, 94° E–105° E). The YERB is the second-longest river in China, which originates from the northern foot of the Bayan Har Mountains on the Tibet Plateau, and flows through nine provinces including Qinghai, Sichuan, Gansu, Ningxia, Inner Mongolia, Shanxi, Shaanxi, Henan, and Shandong. The basin area is 7.95 million km^2 and is about 1900 km long and 1100 km wide. The YERB is a vast territory and contains many mountains, different landforms, and a complicated geographical environment; there is also a great disparity between the east and west [40]. In addition, the YERB is located at middle latitudes, and the effects of atmospheric circulation and monsoon circulation on it are complicated. Therefore, the climate of different regions in the YERB differs significantly, and the annual and seasonal changes of climate elements are large [41]. From west to east, the YERB includes the eastern Tibet Plateau (upstream), Loess Plateau (middle), and North China Plain (downstream), and the east-west altitude difference is 4480 m. Therefore, the study of the optical and physical characteristics of aerosols in different topographic environments of the YERB can help to understand the specific characteristics of aerosols and can provide evidence for the study of aerosol radiation forcing, which is of great scientific significance.

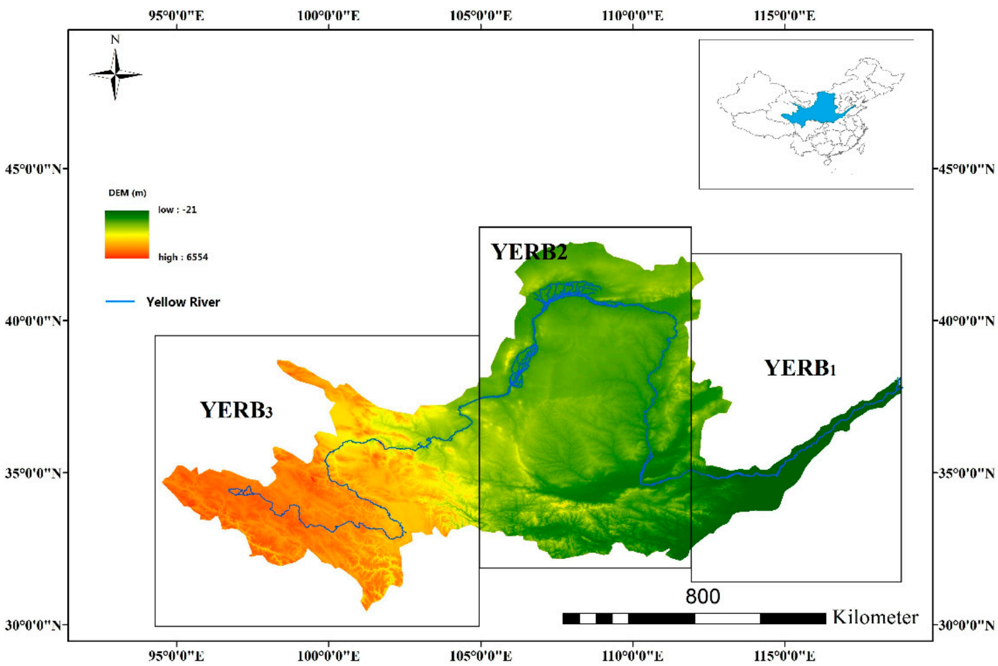

Figure 1. Geographical locations of the Yellow River Basin (YERB). The color bar represents the altitude (elevation).

3. Materials and Methods

CALIPSO is a small earth-probing satellite project jointly carried out by NASA's Langley Research Center (LaRC) and the National Space Research Center of France in 2002 [42]. CALIPSO was launched on 28 April 2006 and can provide not only aerosol and cloud characteristics that vary with latitude and longitude, but also information about the vertical distribution of aerosols and clouds. CALIPSO can identify aerosol types and cloud water/ice phase states and can obtain vital data such as radiation flux and atmospheric state. This data can be used to assess the impact of aerosols and clouds on radiation, and thus improve the ability to predict climate change [43,44]. The orbital altitude of the CALIPSO satellite is 705 km and the dip angle is 98.2°, which has the advantage of a wide field of view. CALIOP is the most important piece of detection equipment on the CALIPSO satellite, including the laser transmitting and receiving system, which is located on a T-type optical platform, thus ensuring the stability of the system. The CALIOP telescope receives backscattered signals divided into three channels. One channel measures the backscattering intensity of 1064 nm, while the other two channels measure the orthogonal polarization backscattering signal of 532 nm. CALIOP can obtain the backscattering coefficients of two wavelengths (532 and 1064 nm) during the day and night, and can also provide vertical profiles of the 532-nm volume depolarization ratio, which is the ratio of the 532-nm vertical backscattering intensity to the 532-nm parallel backscattering intensity. It reflects the irregularity in the measured particles. CALIOP can also provide the color ratio, which is the ratio of the 1064-nm backscattering intensity to the 532-nm total backscattering intensity. The size of the particles can be identified by this color ratio [45,46]. The CALIPSO dataset is processed, stored in a hierarchical data format, and released by the Atmospheric Sciences Data Center of Langley.

CALIPSO datasets are mainly composed of two levels, i.e., Level 1 and Level 2 data products [44], whereas, in this study, Level 2 aerosol layer products at 532 nm were used. The CALIPSO aerosol Level 2 products include aerosol layers, aerosol classifications, and aerosol profile products. The horizontal resolution of the aerosol layer products is 5 km, and the revisit time is 16 days. The aerosol layer products are generated based on the raw CALIPSO profile data using the selective iterated boundary locator (SIBYL) algorithm. Using SIBYL, the feature layers are detected in each raw profile data, and then the amount (number) of aerosol feature layers (N), and the height of the feature layer's base (HB_N) and top (HT_N) is obtained. The data contain at most eight vertical layers ($N \leq 8$) in the whole atmosphere in every raw profile data. During the next time, the Scene Classification Algorithm (SCA) is applied on each vertical layer to classify into six different species, including clean marine aerosol, dust aerosol, polluted continent aerosol, clean continent aerosol, polluted dust aerosol, and smoke aerosol. Different species in different layers are endowed with different LiDAR ratios and retrieved to extinction coefficient $\delta(z)$ and backscatter coefficient $\beta(z)$ profiles based on Hybrid Extinction Retrieval Algorithms (HERAs). Each raw profile dataset has different aerosol feature layers, and each feature layer has an extinction coefficient profile. Hence, the aerosol optical depth (AOD) of the Nth aerosol layer (AOD_N) is calculated as the integral of the extinction coefficient in different layers (Equation (1)). Then, the integrated volume depolarization ratio of the Nth aerosol layer (DR_N) and the integrated attenuated total color ratio of the Nth aerosol layer (CR_N) can also be calculated using Equations (2) and (3), respectively. The uncertainty analysis of AOD_N, DR_N, and CR_N are also performed based on a relative error, and the results are stored in the data products with respect to different quality flags. In this study, only the highest quality (uncertainty ≤ 3) datasets were considered and resampled at $1° \times 1°$ spatial resolution.

This study aimed to explore the vertical physical and optical characteristics of the aerosol layers, and the variables used include the amount (number) of aerosol feature layers (N), the height of the highest aerosol layer top (HT_H), the height of the highest aerosol layer base (HB_H), the AOD of the Nth aerosol layer (AOD_N), the sum of the AOD from all the aerosol layers (AODs, Equation (4)), the AOD proportion of the nth aerosol layer ($PAOD_N$, Equation (5)), the integrated volume depolarization ratio of the Nth aerosol layer (DR_N), and the integrated attenuated total color ratio of the Nth aerosol layer (CR_N). The details of every variable can be found in Abbreviations.

$$AOD_N = \int_{HT_N}^{HB_N} \delta(z)dz;\ N = 1, 2, \ldots, 7, 8 \tag{1}$$

$$DR_N = \frac{\sum_{HT_N}^{HB_N} \beta_{532,\perp}(z)}{\sum_{HT_N}^{HB_N} \beta_{532,\parallel}(z)};\ N = 1, 2, \ldots, 7, 8 \tag{2}$$

$$CR_N = \frac{\sum_{HT_N}^{HB_N} \beta_{1064}(z)}{\sum_{HT_N}^{HB_N} \beta_{532}(z)};\ N = 1, 2, \ldots, 7, 8 \tag{3}$$

$$AOD_s = \sum\nolimits_1^N AOD_N;\ N = 1, 2, \ldots, 7, 8 \tag{4}$$

$$PAOD_N = \frac{AOD_N}{AOD_s};\ N = 1, 2, \ldots, 7, 8 \tag{5}$$

In this study, the AOD of the lowest aerosol layer (AOD_1) and the AOD proportion of the lowest aerosol layer ($PAOD_1$) were mainly analyzed in the next section. The mean annual and seasonal values of each variable over the different sub-regions of the YERB were calculated to investigate the interannual and seasonal variations and characteristics of the aerosol layers.

4. Results and Discussions

4.1. Interannual Variations and Characteristics of Aerosol Layers over the YERB

Figure 2a shows that the annual mean values of AOD_S were high over the $YERB_1$ (0.4–0.6) compared to the $YERB_2$ (0.2–0.3) and $YERB_3$ (0.1–0.2) regions. This might be due to a large urban population, relatively developed economy, and large aerosol emissions, as $YERB_1$ is located in the North China Plain (NCP) [47] and close to urban agglomerations of the BTH region, which is one of the most polluted regions with high aerosol contents in China [48,49]. These results are consistent with the previous study, which has reported a mean AOD mean value of 0.5 over the Beijing and XiangHe AERONET sites [50]. $YERB_3$ is located in the upstream region of the YERB, including the eastern Tibet Plateau, which is sparsely populated; therefore, low aerosol contents were expected [51–53]. The previous study of aerosol layers over the Tibet Plateau has reported mean AOD values less than 0.2 due to low aerosol loadings over the region [54]. Annual mean AOD values were between 0.2 and 0.3 over the $YERB_2$, which were close to those observed at the Semi-Arid Climate and Environment Observatory of Lanzhou University (SACOL) station. At SACOL, AOD observations from a sky radiometer were between the 0.2 and 0.4 range at SACOL station during spring [55], and annual mean AOD was observed between 0.3 and 0.4 at SACOL [56]. AOD values at SACOL represented the single point location, whereas the AOD over $YERB_2$ was the average of a specific region, which might be the reason for differences between annual mean AOD values at SCAOL and $YERB_2$. Furthermore, the geographical environment of SACOL is a semi-arid climate with high-frequency sandstorms. Thus, the AOD values are slightly higher in SACOL compared to the values observed over the $YERB_2$ [57].

The values of N exhibit strong regional characteristics (Figure 2b). The highest values of N (2.1 to 2.4) were observed over the $YERB_1$ compared to the $YERB_2$ (1.7–2.0) and $YERB_3$ (1.4–1.6). This might have happened as $YERB_1$ is located in the monsoon climate region; the air temperature is relatively high and the atmosphere aerosol loadings are relatively large, which might lead to aerosol vertical stratifications in the atmosphere [58,59]. However, $YERB_3$ is located at the eastern edge of the Tibet Plateau, and the underlying surfaces are mainly composed of mountains and plateaus, where aerosol loadings are relatively low, and the air temperature also remains low [60]. Thus, this scenario might have very little chance for aerosol vertical stratifications in the atmosphere. Therefore, low values of N were observed over the $YERB_3$.

The HT_H vary significantly with respect to the topography of the three sub-regions; i.e., $YERB_3$ has relatively high altitudes because of the plateaus and mountains (Figure 2c). Therefore, the annual mean values of HT_H were between 6.0 and 7.5 km over the $YERB_3$ followed by $YERB_2$ (4.5–5.5 km) and $YERB_1$ (3.5–5 km).

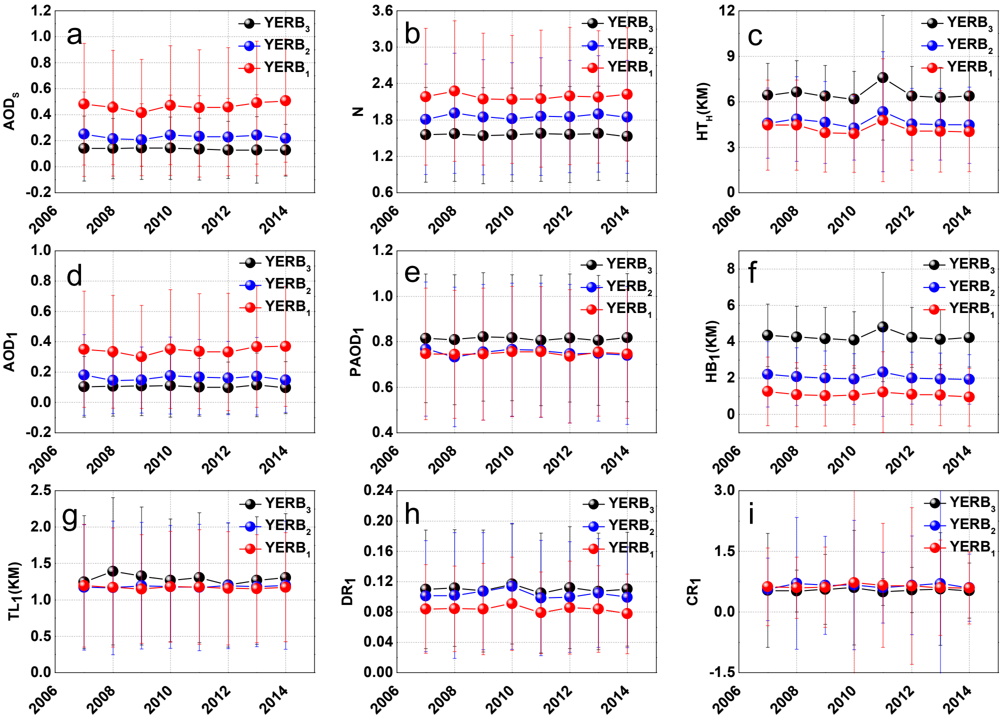

Figure 2. Interannual variation in optical and physical properties of the lowest aerosol layers in three sub-regions of the Yellow River Basin (YERB): (**a**) sum of aerosol optical depths (AODs) from all aerosol layers, (**b**) amount (number) of aerosol feature layers (N), (**c**) height of the highest aerosol layer top (HT_H), (**d**) AOD of the lowest aerosol layer (AOD_1), (**e**) AOD proportion of the lowest aerosol layer ($PAOD_1$), (**f**) height of the lowest aerosol layer base (HB_1), (**g**) thickness of the lowest aerosol layer (TL_1), (**h**) depolarization ratio of the lowest aerosol layer (DR_1), and (**i**) color ratio of the lowest aerosol layer (CR_1), from January 2007 to December 2014 (the wavelength is 532 nm).

Similar to the integrated AOD, the highest values of AOD_1 (0.3–0.4) were observed over $YERB_1$ compared to the $YERB_2$ (0.1–0.2) and $YERB_3$ (~0.1) (Figure 2d). Figure 2e shows that the $PAOD_1$ values were very large (0.7 to 0.85) over all the sub-regions, which indicates that atmospheric aerosols were mainly concentrated in the bottom atmospheric layer. The $PAOD_1$ values over $YERB_3$ (0.8–0.85) were large compared to $YERB_2$ (0.72–0.77) and $YERB_1$ (0.72–0.75). This phenomenon might be due to the high altitudes and low temperatures in the $YERB_3$ region, or due to the weak effects of aerosol vertical convection and aerosol stratification [53,54,60]. Figure 2f shows that the values of HB_1 significantly change with respect to the topography, as the highest values of HB_1 (4–5 km) were observed over the $YERB_3$ region compared to the $YERB_2$ (2–3 km) and $YERB_1$ (1–2 km) regions. As shown in Figure 2g, the values of TL_1 were slightly higher over $YERB_3$ (1.2–1.4 km) than those observed over the $YERB_2$ (1.15–1.2 km) and $YERB_1$ (1.14–1.2 km) regions. This might be due to the vertical convection effects and stratifications of the aerosol layer, which were stronger over $YERB_1$ and $YERB_2$ than $YERB_3$ [56–59].

The aerosol layer-integrated volume depolarization ratio can reflect the non-spherical characteristics of aerosol particles. Higher values of DR_1 (0.095–0.12) were observed over $YERB_3$ and $YERB_2$, indicating the non-spherical characteristics of the lowest aerosol layers. This might be because of dust aerosols, which occur more frequently in the eastern edge of the Tibet Plateau ($YERB_3$) and the Loess plateau ($YERB_2$), leading to more priority being given to those aerosol types regarding the dust over those regions [53–57]. In addition, the shapes of the dust particles are non-spherical; therefore, DR_1 values were large over these regions. These results were consistent with the previous study [61]. Further, small values of DR_1 (0.07–0.09) were small over the $YERB_1$, indicating spherical characteristics of the lowest aerosol layers. The aerosol layer-integrated attenuated total color ratio can reflect the size of the aerosol layer particles. Figure 2i shows the interannual variations in the integrated attenuated total color ratio of the lowest aerosol layers (CR_1) over the YERB. The CR_1 values were lower (0.45–0.6) over $YERB_3$ than those observed over $YERB_2$ (0.55–0.7) and $YERB_1$ (0.6–0.7). These results suggested that the lowest aerosol layer contains aerosol particles with a small size over $YERB_3$ compared to $YERB_2$ and $YERB_1$. This might be because the aerosol loadings of the eastern main body of the Tibet Plateau ($YERB_3$) are low all year round [53,54].

4.2. Seasonal Variations and Characteristics of Aerosol Layers over the YERB

Seasonal variations were analyzed in AOD_S over the three sub-regions of the YERB (Figures 3a and 4a,b). During each season, the seasonal mean AOD_S values were high over the $YERB_1$ (0.4–0.6) region compared to the $YERB_3$ (0.12–0.2) region. This might be due to the regional effects, as the $YERB_1$ at the North China Plain (NCP) is close to the BTH, which is a region of high aerosol loadings [24,47–49]. Therefore, the seasonal mean values of AOD_S were high over $YERB_1$. However, $YERB_3$ is located at the eastern Tibet Plateau, which is a region of low aerosol emissions that led to low mean AOD_S values [52,54,60]. Overall, the values of AOD_S were higher in summer (~0.6) (Figure 4b) followed by autumn (~0.5) (Figure 4c), winter (~0.4) (Figure 4d), and spring (~0.4) (Figure 4a) over the $YERB_1$ region. This might be due to the large relative humidity in summer [9,39,62]. Figures 3b and 4e–h show the seasonal variations in N over the three sub-regions of the YERB, and the seasonal mean values of N were greater than or equal to 2 over $YERB_1$ (2.0–3.0) compared to $YERB_2$ (1.7–2.0) and $YERB_3$ (1.4–1.7). $YERB_1$ is located in a region with a temperate monsoon climate, and the atmosphere possesses a stronger vertical movement than that over $YERB_3$ and $YERB_2$, which leads to a clear vertical stratification of the atmosphere and increases the amount of aerosol stratification [50,58,59,63,64]. However, $YERB_3$ is located at the eastern edge of the Tibet Plateau, which is mainly composed of mountains and plateaus with low air temperature and weak atmospheric vertical convection [51,65]. In addition, the values of N were larger in spring (Figure 4e) followed by summer (Figure 4f), autumn (Figure 4g), and winter (Figure 4h). Especially over the $YERB_1$ region, N was significantly greater (~2.5) in spring compared to the other regions. This might be due to high temperature and strong vertical convection, which led to a significant stratification of aerosols, resulting in greater values of N over $YERB_1$ [24,48,49,58]. Similarly, the greater values of N were observed over $YERB_2$ compared to $YERB_3$, which might be due to the frequently occurred sandstorms over the Loess Plateaus and a significant effect of atmospheric convection [55,57].

The seasonal mean values of HT_H (6–7.5 km) over the $YERB_3$ during each season were greater than those values observed over the $YERB_2$ (4–5 km) and $YERB_1$ (3–5 km) due to the high altitudes of the plateaus (Figures 3c and 4i–l) [47,53,54,57]. At the seasonal scale, large values of HT_H were observed in spring and summer, whereas small values were observed in autumn and winter. This might be due to the frequently occurred straw burning phenomena, which led to large aerosol emissions and increased the HT_H [9,63,66].

Similar to the integrated AOD_S, high seasonal mean AOD_1 values were found over the $YERB_1$ compared to the other sub-regions (Figures 3d and 4m–p). At the seasonal scale, seasonal mean values of AOD_1 were higher in summer (~0.4) followed by autumn (~0.38), winter (~0.35), and spring (~0.28) over the $YERB_1$. This might be due to the grain harvest season and straw-burning activities, which frequently occur in summer and autumn [24,47]. The seasonal mean values of $PAOD_1$ were large over the $YERB_1$ region compared to the other sub-regions (Figures 3e and 5a–d). These results indicate that atmospheric aerosols were mainly concentrated in the lowest aerosol layer over the sub-regions.

It was noticed that the $PAOD_1$ slightly decreased over the $YERB_2$ and $YERB_1$ regions in spring and summer, which might be due to the large values of N, as discussed above. However, large values of $PAOD_1$ (0.79–0.83) were observed in autumn and winter over all the sub-regions, which might be due to low temperature and weak vertical convection and aerosol stratification [51,57,58].

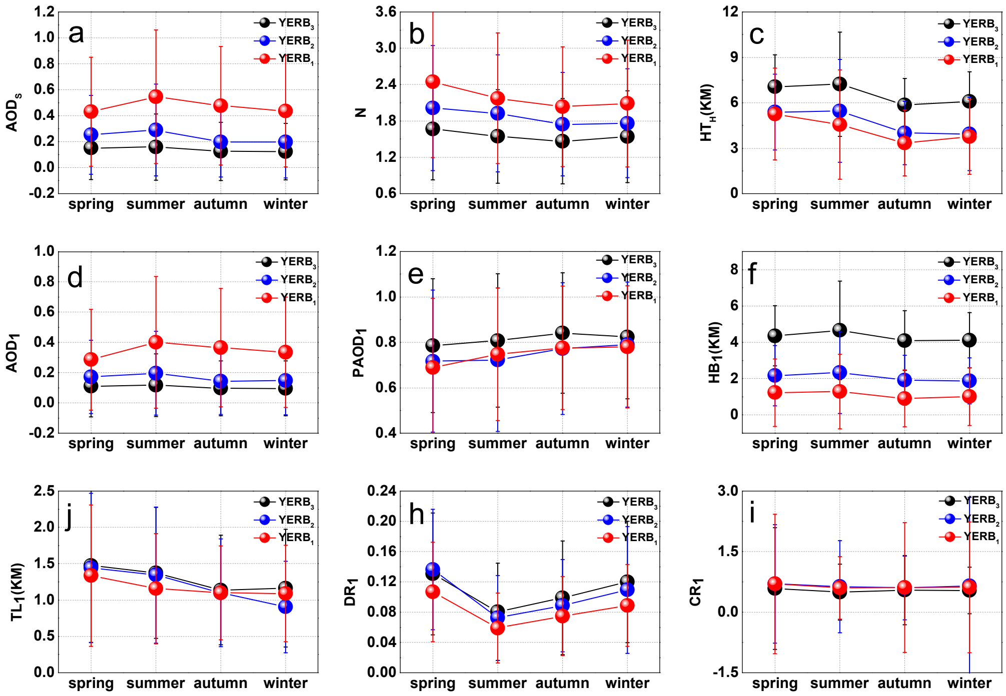

Figure 3. Seasonal variations in optical and physical properties of the lowest aerosol layers in three sub-regions of the YERB: (**a**) AOD_S, (**b**) N, (**c**) HT_H, (**d**) AOD_1, (**e**) $PAOD_1$, (**f**) HB_1, (**g**) TL_1, (**h**) DR_1 and (**i**) CR_1, from January 2007 to December 2014 (the wavelength is 532 nm).

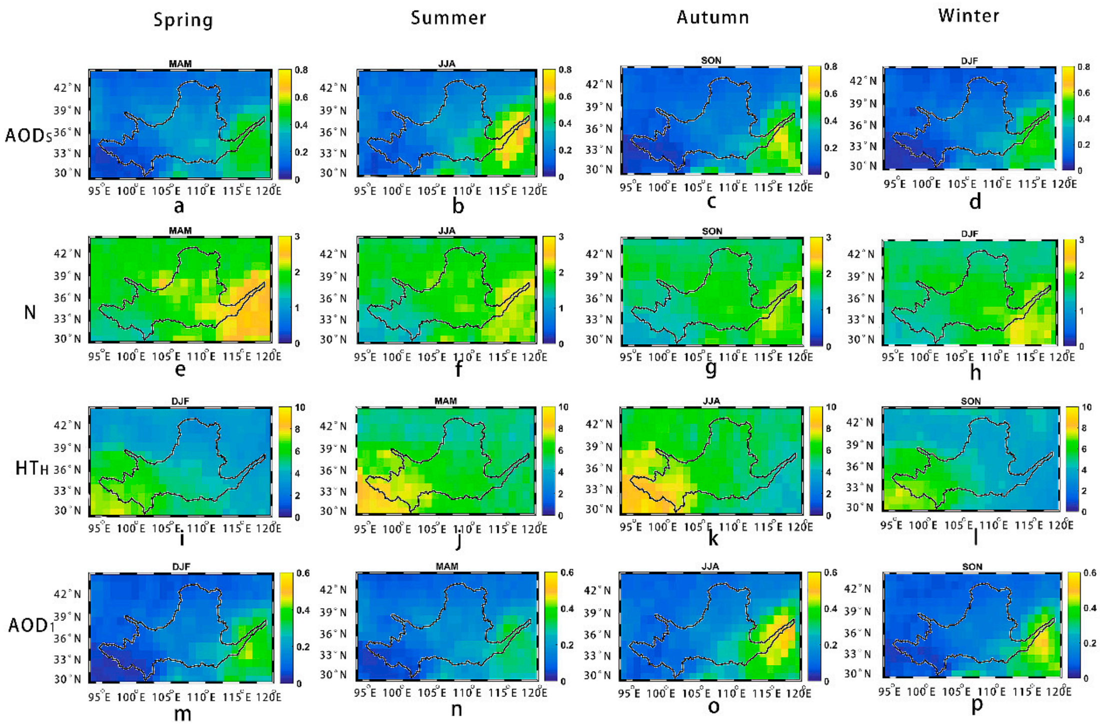

Figure 4. Seasonal distributions of AOD_S (**a**–**d**), N (**e**–**h**), HT_H (**i**–**l**), and AOD_1 (**m**–**p**) over the YERB region.

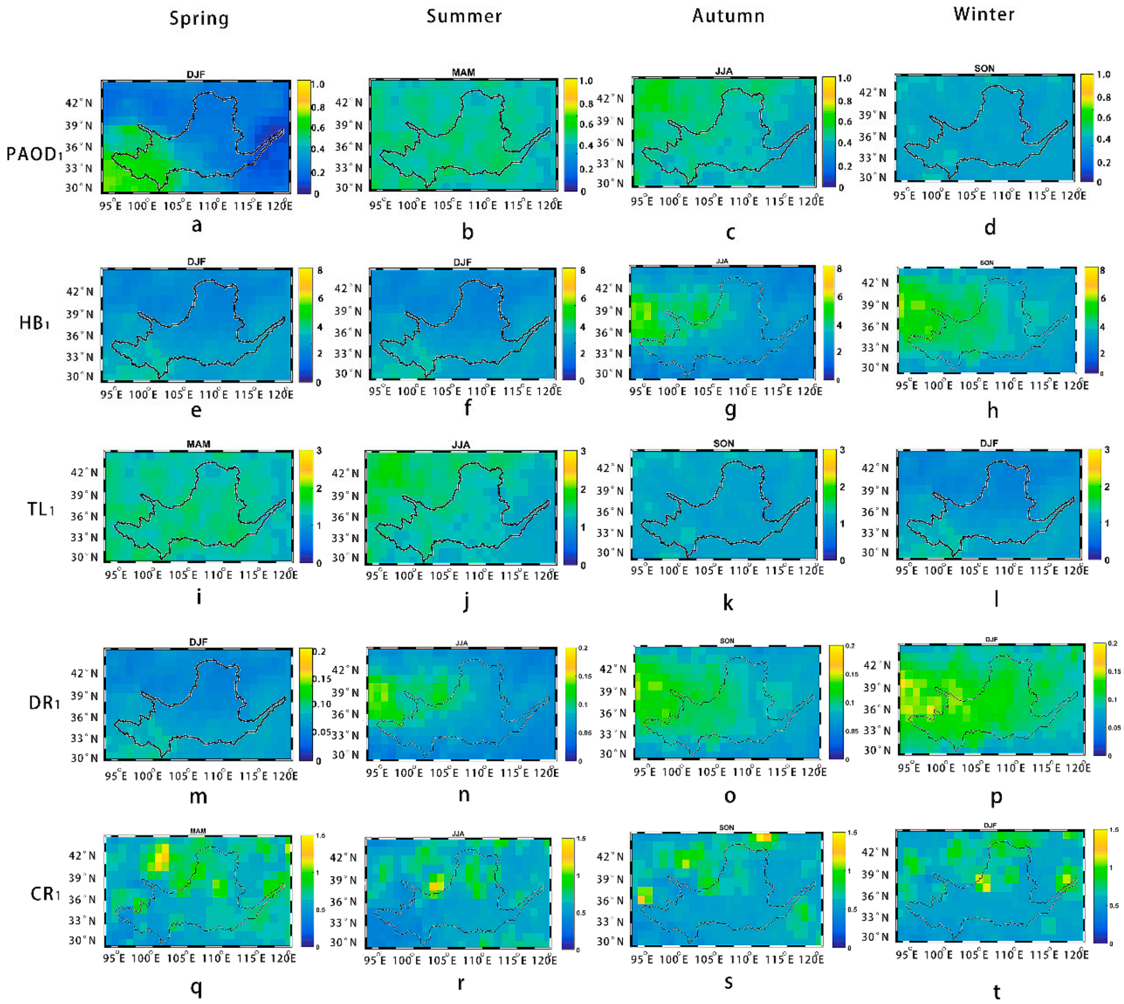

Figure 5. Seasonal distribution of $PAOD_1$ (**a**–**d**), HB_1 (**e**–**h**), TL_1 (**i**–**l**), DR_1 (**m**–**p**), and CR_1 (**q**–**t**) in the YERB.

High seasonal mean values of HB_1 were observed over the $YERB_3$ (4–4.6 km) region compared to the $YERB_2$ (2–2.4 km) and $YERB_1$ (1–1.5 km) regions (Figures 3f and 5e–h). At the seasonal scale, high values of HB_1 were observed in spring and summer, whereas low values were observed in autumn and winter. In spring and summer, air temperature is relatively high compared to autumn and winter with strong vertical convectional effects, which increased the height of the lowest aerosol layer base [58,66]. No significant variations in TL_1 were observed with respect to topographical variations (Figures 3j and 5i–l). Seasonal variations showed large values of TL_1 in spring (1.35 to 1.5 km) followed by summer (1.2–1.4 km), and autumn and winter (0.9–1.2 km).

Seasonal variations showed high values of DR_1 in spring (0.12–0.13) over the $YERB_2$ and $YERB_3$ regions, which indicate the non-spherical characteristics of the lowest aerosol layers. However, lower values were observed in summer (0.06–0.08), autumn (0.07–0.1), and winter (0.09–0.12), which indicates spherical shapes of the aerosols in the lowest aerosol layers. Seasonal variations of CR_1 showed high values in spring (0.7) over the $YERB_1$ and $YERB_2$, which indicate the large size of aerosol particles in the lowest layers. However, relative small values were observed for other seasons, especially over the $YERB_3$ (0.5–0.6).

4.3. The Correlations of the Lowest Aerosol Properties over the YERB

In order to better understand the seasonal spatial characteristics of aerosol layers over the YERB, correlation analyses of aerosol layer parameters are worth studying at seasonal and regional scales, which can help to better understand the causes of spatiotemporal characteristics of aerosol layers over the YERB. Correlation analyses were performed between AOD_1 and TL_1 over each sub-region (Figure 6), which showed the direct relationship, i.e., the thicker the TL_1, the higher the AOD_1. This was consistent with theoretical understanding, as AOD is the integral of extinction coefficients with respect to altitude, so the thicker the TL_1, the greater the integral distances, and the higher the values of AOD_1. According to previously discussed results, AOD_1 was high over the $YERB_1$ region; therefore, a higher correlation was expected over the $YERB_1$. Figure 6 showed a higher correlation (R^2) of 0.59 in spring, 0.58 in summer, 0.78 in autumn, and 0.76 in winter over the $YERB_1$ sub-region compared to the $YERB_2$ and $YERB_3$ regions. These results were consistent and supported by the previous study over the Tibet Plateau [54].

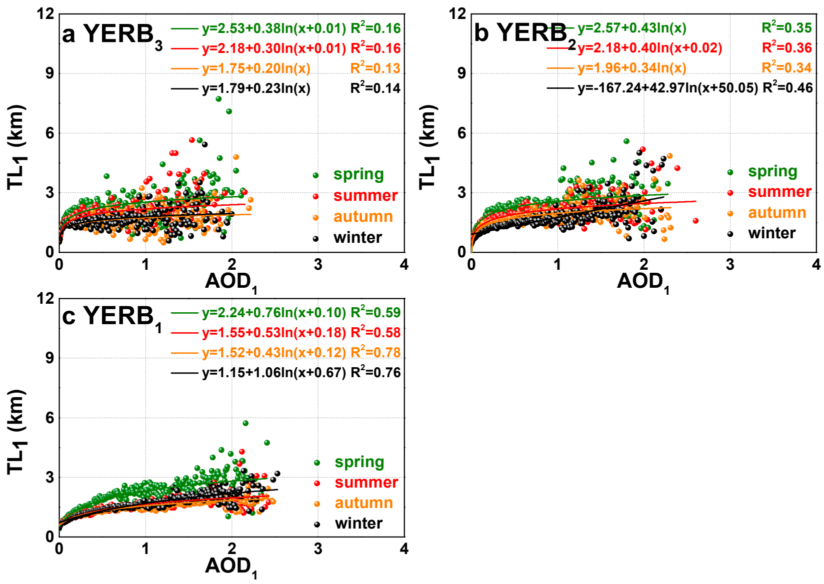

Figure 6. Correlation between AOD of the lowest aerosol layer (AOD_1) and thickness of the lowest aerosol layer (TL_1) over YERB. Where (**a**) is for $YERB_3$, (**b**) is for $YERB_2$, and (**c**) is for $YERB_1$.

Figure 7 showed a significant positive linear correlation ($R^2 \geq 0.90$) between N and HT_H over all the sub-regions of the YERB. These results were expected because of significantly vertically distributed aerosol layers in the whole atmosphere, which led to the higher values of HT_H.

Similarly, a significant negative correlation was observed between N and $PAOD_1$ over the YERB region (Figure 8). This was expected because, for a large amount (number) of aerosol feature layers (N), small values of $PAOD_1$ were observed, which led to a significant negative correlation.

Figure 9 shows the probability distribution scatter diagram between DR_1 and CR_1 over the YERB, and the color bar represents the probability values. It can be noticed that the data points were mainly concentrated in the lower-left corner over each region during each season. The range of DR_1 and CR_1 was between 0 and 0.2, and 0 and 1, respectively. These results indicate smaller particle sizes with non-spherical shapes in the lowest aerosol layers over the whole YERB. However, the CR_1 values over all the sub-regions were generally higher in spring (1–1.5) compared to the other seasons. This might be due to the presence of dust aerosols with large particle sizes over the YERB. It is well-known that dust layers generally exist at high altitudes with large particle sizes with non-spherical characteristics.

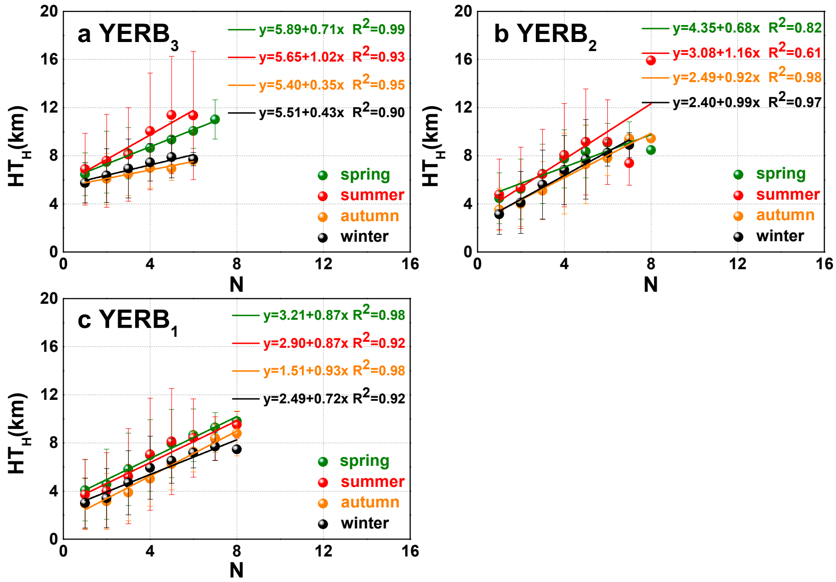

Figure 7. The correlations between the height of the highest aerosol layer top (HT_H) and amount (number) of aerosol feature layers (N) over TP. (**a**) is for $YERB_3$, (**b**) is for $YERB_2$, and (**c**) is for $YERB_1$.

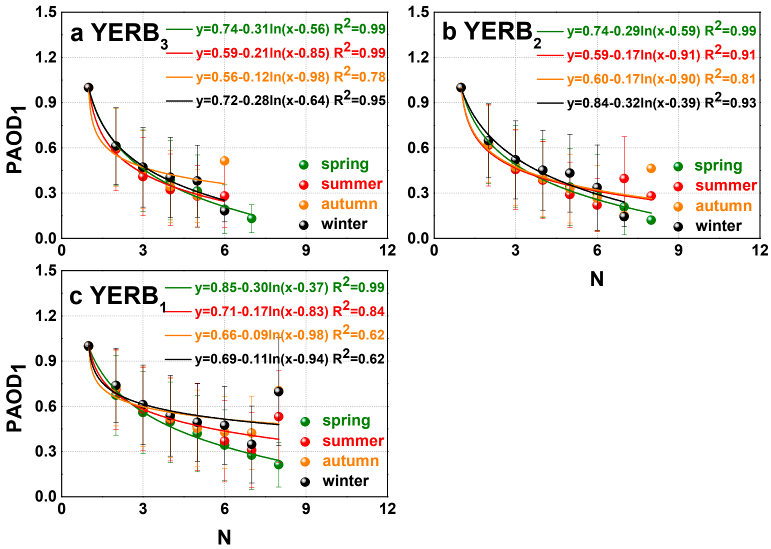

Figure 8. The correlations between $PAOD_1$ and layer amount (N) over TP. Where (**a**) is for $YERB_3$, (**b**) is for $YERB_2$, and (**c**) is for $YERB_1$.

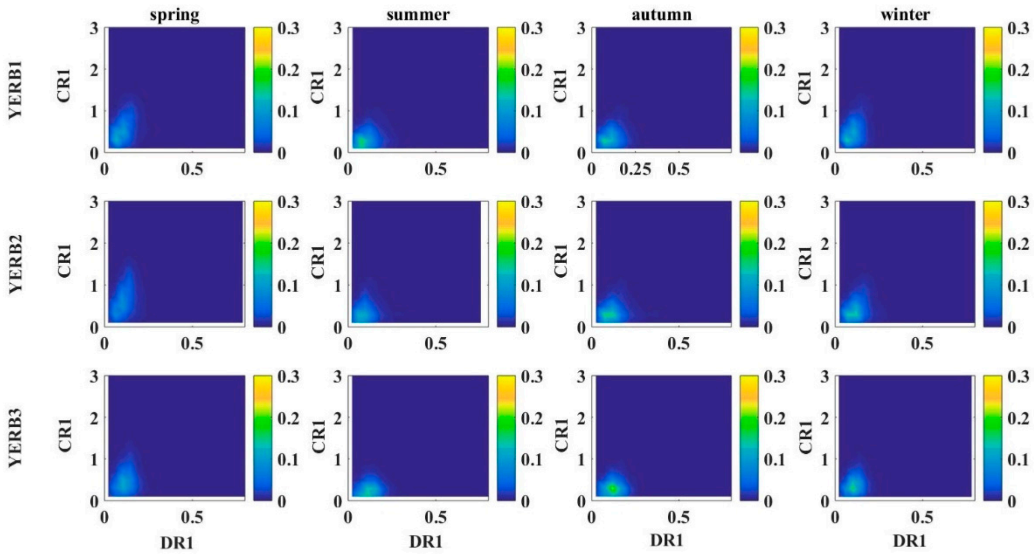

Figure 9. Probability distribution diagram of correlations between DR_1 and CR_1 over YERB.

5. Conclusions

In this study, the optical and physical properties of the aerosol layers over the YERB were investigated using the CALIPSO Level 2 layer products from January 2007 to December 2014. This paper can be a reference to further investigation of the physical and optical properties of aerosols over the YERB or over the other regions. The main outcomes are:

(a) AOD_S values and relative large values of aerosol amount ($N > 2$) were observed over the YERB1 region, as $YERB_1$ is the most polluted region, and the atmosphere possesses strong vertical movement, which can lead to a clear vertical stratification.

(b) High values of the HT_H were observed over the YERB. In addition, the HT_H and the HB_1 significantly vary with respect to the topography and seasons as high values observed in spring and summer compared to autumn and winter. However, the TL_1 did not vary with topographical features, and low values of the TL_1 values (approximately 1–1.5 km) were observed over the YERB.

(c) $PAOD_1$ was quite large (0.7–1.0) over the YERB, which suggested that atmospheric aerosols were primarily concentrated in the bottom layer.

(d) The values of DR_1 (0.15–0.2) and CR_1 (~1) were large over the YERB in spring because of dust aerosols.

(e) A positive correlation between AOD_1 and TL_1 and A and HT_H was observed over the whole YERB, whereas N and $PAOD_1$ showed a significant log-negative correlation.

Overall, this study provides a better understanding of air pollution in the YERB region. In the future study, aerosol types and their microphysical properties over the region will be considered. Also, the vertical feature mask (VFM) products of CALIPSO will be considered to investigate the vertical structure and layer stratification characteristics of different aerosol species.

Author Contributions: M.Z. and J.L. conceived and designed the experiments; M.Z. performed the experiments; J.L. and M.B. analyzed the data; C.Z. contributed analysis tools; M.Z. wrote the paper; M.B., X.X., K.M.K., and F.Z. revised the manuscript.

Funding: This research was funded by the National Natural Science Foundation of China (No. 41801282), the Programs for Science and Technology Development of Henan Province (No. 192102310008), the Key Scientific Research Project of Henan Institutions of Higher Learning (No. 18B170007), the Nanyang Normal University Scientific Research Project (No. ZX2017014), the Science and Technology Project of Nanyang City (No. 2017JCQY017), the Special Project of Jiangsu Distinguished Professor (No. 1421061801003 and 1421061901001), and the Deanship of Scientific Research, King Khalid University, Kingdom of Saudi Arabia (RGP2/54/40).

Acknowledgments: We also thank the NASA Langley Research Center for providing the experimental data. We will also like to thank the editors for modifying and revising this manuscript.

Conflicts of Interest: The authors declare no conflict of interest.

Abbreviations

The following abbreviations are used in this manuscript:

Lon	longitude
Lat	latitude
AOD_N	The AOD of the nth aerosol layer; N = 1, 2, ... , 7, 8
AOD_S	The sum of AODs from all aerosol layers
HT_N	The height of the nth aerosol layer top; N = 1, 2, ... , 7, 8
HB_N	The height of the nth aerosol layer base; N = 1, 2, ... , 7, 8
HT_H	The height of the highest aerosol layer top
TL_N	The thickness of the nth aerosol layer; N = 1, 2, ... , 7, 8
N	The amounts of all aerosol layers
$PAOD_N$	The AOD proportion of the nth aerosol layer; N = 1, 2, ... , 7, 8
DR_N	The integrated volume depolarization ratio of the nth aerosol layer; N = 1, 2, ... , 7, 8
CR_N	The integrated attenuated total color ratio of the nth aerosol layer; N = 1, 2, ... , 7, 8

References

1. Hinds, W.C. *Aerosol Technology*; Wiley & Sons: Hoboken, NJ, USA, 2000; Volume 31, p. 175.
2. Kulmala, M.; Kontkanen, J.; Junninen, H.; Lehtipalo, K.; Manninen, H.E.; Nieminen, T.; Petäjä, T.; Sipilä, M.; Schobesberger, S.; Rantala, P.; et al. Direct Observations of Atmospheric Aerosol Nucleation. *Science* **2013**, *339*, 943–946. [CrossRef]
3. Mcmurry, P.H. A review of atmospheric aerosol measurements. *Atmos. Environ.* **2000**, *34*, 1959–1999. [CrossRef]
4. Qin, Y.; Oduyemi, K. Atmospheric aerosol source identification and estimates of source contributions to air pollution in Dundee, UK. *Atmos. Environ.* **2003**, *37*, 1799–1809. [CrossRef]
5. Rogge, W.F.; Hildemann, L.M.; Mazurek, M.A.; Cass, G.R.; Simoneit, B.R.T. Sources of fine organic aerosol. 5. Natural gas home appliances. *Environ. Sci. Technol.* **1993**, *27*, 2736–2744. [CrossRef]
6. Wolfgang, F.; Rogge, L.M.H.; Mazurek, A.M.; Cass, G.R.; Simoneit, B.R.T. Sources of fine organic aerosol. 7. Hot asphalt roofing tar pot fumes. *Environ. Sci. Technol.* **1997**, *31*, 2726–2730.
7. Han, G.; Xu, H.; Gong, W.; Liu, J.; Du, J.; Ma, X.; Liang, A. Feasibility Study on Measuring Atmospheric CO2 in Urban Areas Using Spaceborne CO2-IPDA LIDAR. *Remote Sens.* **2018**, *10*, 985. [CrossRef]
8. Ge, H.; Xin, M.; Ailin, L.; Tianhao, Z.; Yannan, Z.; Miao, Z.; Wei, G. Performance evaluation for china's planned co2-ipda. *Remote Sens.* **2017**, *9*, 768.
9. Zhang, M.; Ma, Y.; Gong, W.; Zhu, Z. Aerosol Optical Properties of a Haze Episode in Wuhan Based on Ground-Based and Satellite Observations. *Atmosphere* **2014**, *5*, 699–719. [CrossRef]
10. Gong, W.; Zhang, M.; Han, G.; Ma, X.; Zhu, Z. An Investigation of Aerosol Scattering and Absorption Properties in Wuhan, Central China. *Atmosphere* **2015**, *6*, 503–520. [CrossRef]
11. Kaiser, J.; Granmar, M. Mounting evidence indicts fine-particle pollution. *Science* **2005**, *307*, 1858–1861. [CrossRef]
12. Magistrale, P.V. *Health Aspects of Air Pollution*; Springer: Berlin/Heidelberg, Germany, 1992; pp. 25–31.
13. Tie, X.; Wu, D.; Brasseur, G. Lung cancer mortality and exposure to atmospheric aerosol particles inguangzhou, china. *Atmos. Environ.* **2009**, *43*, 2375–2377. [CrossRef]
14. Edenhofer, O.; Seyboth, K. Intergovernmental Panel on Climate Change (IPCC). *Encycl. Energy Nat. Resour. Environ. Econ.* **2013**, *26*, 48–56.
15. Edenhofer, O. *Climate Change 2014: Mitigation of Climate Change: Working Group iii Contribution to the Fifth Assessment Report of the Intergovernmental Panel on Climate Change*; Cambridge University Press: Cambridge, UK, 2014.
16. Rosenfeld, D. Suppression of Rain and Snow by Urban and Industrial Air Pollution. *Science* **2000**, *287*, 1793–1796. [CrossRef] [PubMed]

17. Twomey, S. The Influence of Pollution on the Shortwave Albedo of Clouds. *J. Atmos. Sci.* **1977**, *34*, 1149–1152. [CrossRef]
18. Parrish, D.D.; Tong, Z. Climate change. Clean air for megacities. *Science* **2009**, *326*, 674–675. [CrossRef]
19. Shen, X.L.; Dang, T.G.; Liu, J. Summary of Beijing-Tianjin-Hebei Haze Causes and Solutions Research. *Adv. Mater. Res.* **2014**, *1010*, 639–644. [CrossRef]
20. Gao, Y.; Zhang, M.; Liu, Z.; Wang, L.; Wang, P.; Xia, X.; Tao, M.; Zhu, L. Modeling the feedback between aerosol and meteorological variables in the atmospheric boundary layer during a severe fog–haze event over the North China Plain. *Atmos. Chem. Phys. Discuss.* **2015**, *15*, 4279–4295. [CrossRef]
21. Dui, W.U.; Liao, B.; Chen, H.; Cheng, W.U. Advances in studies of haze weather over pearl river delta. *Clim. Environ. Res.* **2014**, *19*, 248–264. (In Chinese)
22. Liu, Y. Accessing the Impact of Sea-Salt Emissions on Aerosol Chemical Formation and Deposition over Pearl River Delta, China. *Aerosol Air Qual. Res.* **2015**, *15*, 329–340. [CrossRef]
23. Shen, X.; Sun, J.; Zhang, X.; Zhang, Y.; Zhang, L.; Che, H.; Ma, Q.; Yu, X.; Yue, Y.; Zhang, Y. Characterization of submicron aerosols and effect on visibility during a severe haze-fog episode in Yangtze River Delta, China. *Atmos. Environ.* **2015**, *120*, 307–316. [CrossRef]
24. Bilal, M.; Nichol, J.E. Evaluation of MODIS aerosol retrieval algorithms over the Beijing-Tianjin-Hebei region during low to very high pollution events. *J. Geophys. Res. Atmos.* **2015**, *120*, 7941–7957. [CrossRef]
25. Holben, B.; Eck, T.; Slutsker, I.; Tanre, D.; Buis, J.; Setzer, A.; Vermote, E.; Reagan, J.; Kaufman, Y.; Nakajima, T.; et al. AERONET—A Federated Instrument Network and Data Archive for Aerosol Characterization. *Remote Sens. Environ.* **1998**, *66*, 1–16. [CrossRef]
26. Dubovik, O.; Smirnov, A.; Holben, B.N.; King, M.D.; Kaufman, Y.J.; Eck, T.F.; Slutsker, I. Accuracy assessments of aerosol optical properties retrieved from Aerosol Robotic Network (AERONET) Sun and sky radiance measurements. *J. Geophys. Res. Space Phys.* **2000**, *105*, 9791–9806. [CrossRef]
27. Holben, B.N.; Eck, T.F.; Slutsker, I.; Chatenet, B.; Smirnov, A.; Pinker, R.T. Diurnal variability of aerosol optical depth observed at AERONET (Aerosol Robotic Network) sites. *Geophys. Res. Lett.* **2002**, *29*, 1–30.
28. Omar, A.H.; Won, J.; Winker, D.M.; Yoon, S.; Dubovik, O.; McCormick, M.P. Development of global aerosol models using cluster analysis of Aerosol Robotic Network (AERONET) measurements. *J. Geophys. Res. Space Phys.* **2005**, *110*, 10–14. [CrossRef]
29. Gong, W.; Zhu, Z.; Li, P.; Qin, Q. Mobile aerosol lidar for earth observation atmospheric correction. In Proceedings of the IEEE International Conference on Geoscience and Remote Sensing Symposium, Denver, CO, USA, 31 July–4 August 2006; pp. 1126–1129.
30. Han, D.W.; Liu, W.Q.; Zhang, Y.J.; Lu, Y.H.; Liu, J.G.; Yu, T. An atmospheric aerosol lidar and its experiment in beijing. In Proceedings of the Semiconductor Lasers and Applications III, Beijing, China, 12–13 November 2007.
31. Hamilton, P. Lidar measurement of backscatter and attenuation of atmospheric aerosol. *Atmos. Environ.* **1969**, *3*, 221–223. [CrossRef]
32. Karasiński, G.; Kardaś, A.E.; Markowicz, K.; Malinowski, S.P.; Stacewicz, T.; Stelmaszczyk, K.; Chudzyński, S.; Skubiszak, W.; Posyniak, M.; Jagodnicka, A.K.; et al. LIDAR investigation of properties of atmospheric aerosol. *Eur. Phys. J. Spéc. Top.* **2007**, *144*, 129–138. [CrossRef]
33. Devara, P.; Raj, P.E.; Sharma, S. Remote sensing of atmospheric aerosol in the nocturnal boundary layer using lidar. *Environ. Pollut.* **1994**, *85*, 97–102. [CrossRef]
34. Ansmann, A.; Müller, D. Lidar and Atmospheric Aerosol Particles. *Lidar* **2006**, *102*, 105–141.
35. Cohen, A.; Kleiman, M. On the Measurement of Atmospheric Aerosol Concentration by a Lidar. *J. Appl. Meteorol.* **1978**, *17*, 234–235. [CrossRef]
36. Winker, D.M.; Pelon, J.R.; Mccormick, M.P. The calipso mission: Spaceborne lidar for observation of aerosols and clouds. *Bull. Am. Meteorol. Soc.* **2010**, *91*, 1211–1229. [CrossRef]
37. Winker, D.M.; Hunt, W.H.; McGill, M.J. Initial performance assessment of CALIOP. *Geophys. Res. Lett.* **2007**, *34*, 228–262. [CrossRef]
38. Che, H.; Zhang, X.-Y.; Xia, X.; Goloub, P.; Holben, B.; Zhao, H.; Wang, Y.; Zhang, X.-C.; Wang, H.; Blarel, L.; et al. Ground-based aerosol climatology of China: Aerosol optical depths from the China Aerosol Remote Sensing Network (CARSNET) 2002–2013. *Atmos. Chem. Phys. Discuss.* **2015**, *15*, 7619–7652. [CrossRef]
39. Che, H.; Zhang, X.; Chen, H.; Damiri, B.; Goloub, P.; Li, Z.; Zhang, X.; Wei, Y.; Zhou, H.; Dong, F.; et al. Instrument calibration and aerosol optical depth validation of the China Aerosol Remote Sensing Network. *J. Geophys. Res. Space Phys.* **2009**, *114*, 03206. [CrossRef]

40. Wang, H.; Yang, Z.; Saito, Y.; Liu, J.P.; Sun, X.; Wang, Y. Stepwise decreases of the Huanghe (Yellow River) sediment load (1950–2005): Impacts of climate change and human activities. *Glob. Planet. Chang.* **2007**, *57*, 331–354. [CrossRef]
41. Shen, X.; Sun, J.; Zhang, Y.; Weijun, L.I.; Chi, J.; Zhang, L.; Fan, R. The characteristics of atmospheric aerosol particle number size distribution in arctic yellow river station influenced by long-range transport of autumn air mass. *J. Glaciol. Geocryol.* **2016**. [CrossRef]
42. Winker, D.M.; Pelon, J. The Calipso Mission. In Proceedings of the 2003 IEEE International Geoscience and Remote Sensing Symposium (IGARSS '03), Toulouse, France, 21–25 July 2004; Volume 1322, pp. 1329–1331.
43. Winker, D.M.; Pelon, J.R.; McCormick, M.P. The CALIPSO mission: Spaceborne lidar for observation of aerosols and clouds. In Proceedings of the Third International Asia-Pacific Environmental Remote Sensing Remote Sensing of the Atmosphere, Ocean, Environment, and Space, Hangzhou, China, 23–27 OCtober 2003; pp. 1–11.
44. Winker, D.M.; Vaughan, M.A.; Omar, A.; Hu, Y.; Powell, K.A.; Liu, Z.; Hunt, W.H.; Young, S.A. Overview of the CALIPSO Mission and CALIOP Data Processing Algorithms. *J. Atmos. Ocean. Technol.* **2009**, *26*, 2310–2323. [CrossRef]
45. Winker, D.M.; Tackett, J.L.; Getzewich, B.J.; Liu, Z.; Vaughan, M.A.; Rogers, R.R. The global 3-D distribution of tropospheric aerosols as characterized by CALIOP. *Atmos. Chem. Phys. Discuss.* **2013**, *13*, 3345–3361. [CrossRef]
46. Lolli, S.; D'Adderio, L.P.; Campbell, J.R.; Sicard, M.; Welton, E.J.; Binci, A.; Rea, A.; Tokay, A.; Comerón, A.; Barragan, R.; et al. Vertically Resolved Precipitation Intensity Retrieved through a Synergy between the Ground-Based NASA MPLNET Lidar Network Measurements, Surface Disdrometer Datasets and an Analytical Model Solution. *Remote Sens.* **2018**, *10*, 1102. [CrossRef]
47. Che, H.; Xia, X.; Zhu, J.; Li, Z.; Dubovik, O.; Holben, B.; Goloub, P.; Chen, H.; Estelles, V.; Cuevas-Agulló, E.; et al. Column aerosol optical properties and aerosol radiative forcing during a serious haze-fog month over North China Plain in 2013 based on ground-based sunphotometer measurements. *Atmos. Chem. Phys. Discuss.* **2014**, *14*, 2125–2138. [CrossRef]
48. Wang, L.; Liu, Z.; Sun, Y.; Ji, D.; Wang, Y. Long-range transport and regional sources of PM2.5 in Beijing based on long-term observations from 2005 to 2010. *Atmos. Res.* **2015**, *157*, 37–48. [CrossRef]
49. Tang, G.; Zhu, X.; Hu, B.; Xin, J.; Wang, L.; Münkel, C.; Mao, G.; Wang, Y. Impact of emission controls on air quality in Beijing during APEC 2014: Lidar ceilometer observations. *Atmos. Chem. Phys. Discuss.* **2015**, *15*, 12667–12680. [CrossRef]
50. Fan, X.; Xia, X.A.; Chen, H. Comparison of column-integrated aerosol optical and physical properties in an urban and suburban site on the north china plain. *Adv. Atmos. Sci.* **2015**, *32*, 477–486. [CrossRef]
51. Liu, B.; Cong, Z.; Wang, Y.; Xin, J.; Wan, X.; Pan, Y.; Liu, Z.; Wang, Y.; Zhang, G.; Wang, Z.; et al. Background aerosol over the Himalayas and Tibetan Plateau: Observed characteristics of aerosol mass loading. *Atmos. Chem. Phys. Discuss.* **2017**, *17*, 449–463. [CrossRef]
52. Li, C.; Bosch, C.; Kang, S.; Andersson, A.; Chen, P.; Zhang, Q.; Cong, Z.; Chen, B.; Qin, D.; Gustafsson, Ö. Sources of black carbon to the Himalayan–Tibetan Plateau glaciers. *Nat. Commun.* **2016**, *7*, 12574. [CrossRef]
53. Xu, C.; Ma, Y.M.; You, C.; Zhu, Z.K. The regional distribution characteristics of aerosol optical depth over the Tibetan Plateau. *Atmos. Chem. Phys. Discuss.* **2015**, *15*, 12065–12078. [CrossRef]
54. Zhang, M.; Wang, L.; Bilal, M.; Gong, W.; Zhang, Z.; Guo, G. The Characteristics of the Aerosol Optical Depth within the Lowest Aerosol Layer over the Tibetan Plateau from 2007 to 2014. *Remote Sens.* **2018**, *10*, 696. [CrossRef]
55. Liu, Y.; Huang, J.; Shi, G.; Takamura, T.; Khatri, P.; Bi, J.; Shi, J.; Wang, T.; Wang, X.; Zhang, B. Aerosol optical properties determined from sky-radiometer over Loess Plateau of Northwest China. *Atmos. Chem. Phys. Discuss.* **2011**, *11*, 23883–23910. [CrossRef]
56. Bi, J.; Huang, J.; Fu, Q.; Wang, X.; Shi, J.; Zhang, W.; Huang, Z.; Zhang, B. Toward characterization of the aerosol optical properties over Loess Plateau of Northwestern China. *J. Quant. Spectrosc. Radiat. Transf.* **2011**, *112*, 346–360. [CrossRef]
57. Huang, J.; Zhang, W.; Zuo, J.; Jianrong, B.I.; Shi, J.; Wang, X.; Chang, Z.; Huang, Z.; Yang, S.; Zhang, S. An overview of the semi-arid climate and environment research observatory over the loess plateau. *Adv. Atmos. Sci.* **2008**, *25*, 906. [CrossRef]

58. Wu, Z.; Ma, N.; Gros, J.; Kecorius, S.; Lu, K.; Shang, D.; Wang, Y.; Wu, Y.; Zeng, L.; Hu, M.; et al. Thermodynamic properties of nanoparticles during new particle formation events in the atmosphere of North China Plain. *Atmos. Res.* **2017**, *188*, 55–63. [CrossRef]
59. Zhang, S.; Ma, N.; Kecorius, S.; Wang, P.; Hu, M.; Wang, Z.; Gros, J.; Wu, Z.; Wiedensohler, A. Mixing state of atmospheric particles over the North China Plain. *Atmos. Environ.* **2016**, *125*, 152–164. [CrossRef]
60. Liu, Z.-Y.; Chen, J.-B.; Jin, L.; Zhang, Y.-J.; Lei, C. Roadbed temperature study based on earth-atmosphere coupled system in permafrost regions of the Qinghai-Tibet Plateau. *Cold Reg. Sci. Technol.* **2013**, *86*, 167–176. [CrossRef]
61. Tian, P.; Cao, X.; Zhang, L.; Wang, H.; Shi, J.; Huang, Z.; Zhou, T.; Liu, H. Observation and simulation study of atmospheric aerosol nonsphericity over the Loess Plateau in northwest China. *Atmos. Environ.* **2015**, *117*, 212–219. [CrossRef]
62. Wang, L.; Xin, J.; Li, X.; Wang, Y. The variability of biomass burning and its influence on regional aerosol properties during the wheat harvest season in North China. *Atmos. Res.* **2015**, *157*, 153–163. [CrossRef]
63. Yao, H.; Song, Y.; Liu, M.; Archer-Nicholls, S.; Lowe, D.; McFiggans, G.; Xu, T.; Du, P.; Li, J.; Wu, Y.; et al. Direct radiative effect of carbonaceous aerosols from crop residue burning during the summer harvest season in East China. *Atmos. Chem. Phys. Discuss.* **2017**, *17*, 5205–5219. [CrossRef]
64. Tao, M.; Wang, Z.; Tao, J.; Chen, L.; Wang, J.; Hou, C.; Wang, L.; Xu, X.; Zhu, H. How Do Aerosol Properties Affect the Temporal Variation of MODIS AOD Bias in Eastern China? *Remote Sens.* **2017**, *9*, 800. [CrossRef]
65. Biswas, J.; Pathak, B.; Patadia, F.; Bhuyan, P.K.; Gogoi, M.M.; Babu, S.S. Satellite-retrieved direct radiative forcing of aerosols over North-East India and adjoining areas: Climatology and impact assessment. *Int. J. Clim.* **2017**, *37*, 4756. [CrossRef]
66. Garai, A.; Kleissl, J. Air and Surface Temperature Coupling in the Convective Atmospheric Boundary Layer. *J. Atmos. Sci.* **2011**, *68*, 2945–2954. [CrossRef]